This paper describes objective technical results and analysis. Any subjective views or opinions that might be expressed in the paper do not necessarily represent the views of the U.S. Department of Energy or the United States Government.

SAND2021-4047J

Townsend to Glow Transition for a Nanosecond Pulse Discharge in Helium: Space Charge Formation and Resulting Electric Field Dynamics

Marien Simeni Simeni[1], Yashuang Zheng[1,2], Edward V. Barnat[3] and Peter J. Bruggeman[1,*]

[1]*Department of Mechanical Engineering, University of Minnesota, 111 Church Street SE, Minneapolis 55414 MN, USA*

[2]*State Key Laboratory of Electrical Insulation and Power Equipment, Xi'an Jiaotong University, Xi'an 710049, People's Republic of China*

[3]*Sandia National Laboratories, 1515 Eubank Blvd SE, Albuquerque, NM 87185, USA*

Email: pbruggem@umn.edu

Abstract

Stark polarization spectroscopy is used to investigate the temporal evolution of the electric field distribution in the cathode region of a nanosecond pulsed discharge in helium at 120 Torr. The measurements are performed on the He I transition at 492.19 nm, during the early stages of the discharge formation. The experimental results are compared with the predictions of a 1D fluid model. Time-resolved ICCD images show that the discharge develops as a diffuse, cathode-directed ionization wave with a Townsend-like feature before transitioning to a glow-like structure. Near anode instabilities characterized by filament formation were observed near the high voltage electrode. Within 30 ns, a reduction of the sheath thickness to about 250 µm is observed, coinciding with a gradual increase of the discharge current and proportional increase in electric field at the cathode. The cathode electric field corresponding to this sheath with a thickness of 250 µm is about 40 kV cm^{-1}. A subsequent steep increase of the discharge current leads to a further reduction of the sheath width. The electric field evolution as obtained by the fluid model is in excellent agreement with the measurements and shows that an enhanced ionization near the cathode is causing the space charge formation responsible for the increase in electric field.

1. Introduction

Sheaths are space charge regions at the boundary of a gas phase plasma with a solid surface, whose purpose is to balance the losses of negative and positive particles to walls. At sufficiently low gas pressures, the sheath can be collisionless and the sheath electric fields accelerate positive ions to surfaces resulting in ion energies of several eV up to 100s of eV [1]. However, at near atmospheric pressure, the ion collision mean-free path becomes significantly smaller than the sheath thickness and ions have close to thermal energies [2]. Nonetheless, the significant macroscopic electric fields generated by positive space charges in the sheath remain at atmospheric pressure and will significantly influence the plasma dynamics [2,3].

Many sheath models have been developed including analytical models like the matrix sheath and Child law sheath model [1]. A significant effort of models and measurements have been devoted to developing Bohm velocity criteria for the ion energy when ions are entering the sheath [1, 4].

Sandia National Laboratories is a multimission laboratory managed and operated by National Technology & Engineering Solutions of Sandia, LLC, a wholly owned subsidiary of Honeywell International Inc., for the U.S. Department of Energy's National Nuclear Security Administration under contract DE-NA0003525.

This has been particularly challenging in the case of plasmas with multiple positive ions and in electronegative gases. As an example, Gottscho *et al* performed a comprehensive experimental study of the effects of the presence of electronegative gases, the discharge repetition frequency and the plasma power deposition on the sheath thickness, the electric field profile and motion of the plasma-sheath boundary in glow discharges at 0.3 Torr [5].

A cathode sheath in a dc driven discharge is responsible for the acceleration of electrons generated by ion-induced secondary electron emission on the metal cathode and hence the sustainment of the discharge [1]. Den Hartog *et al* reported spatially resolved electric field measurements in the cathode sheath of a dc driven helium discharge at 3.5 Torr between two metal electrodes [6]. In RF discharges, the sheath thickness varies with the RF cycle and at low pressure stochastic heating becomes an important heating mechanism of electrons by the sheath [1]. A relatively recent review of the sheath theories provides an overview of sheaths in both laboratory and space plasmas [7].

Most of the experimental and computational studies of the electric field profiles in sheaths have been performed in dc and radiofrequency-driven glow discharges [6-11]. The transition from a Townsend to a glow discharge, coinciding with the formation of a sheath, has also been studied extensively [1,12,13]. However, most of the work involved fast imaging and modeling. Ito *et al* performed electric field measurements in parallel plate electrode geometries near breakdown showing a diffuse breakdown on nanosecond time scales inconsistent with a Townsend breakdown mechanism [14]. The breakdown has many similarities with a streamer breakdown but is not filamentary. This diffuse breakdown is enabled by high pre-ionization densities. In this case avalanches overlap and suppress steamer breakdown by smoothing out the electric field, enabling a homogeneous breakdown [2].

The characterization of the formation of a sheath structure in the transition from a Townsend to a glow discharge particularly for nanosecond pulsed discharges, the focus of this work, has received little attention to date. Massines *et al* showed that dielectric barrier discharges (DBDs) could exhibit the features of either Townsend or glow discharges depending on the maximum current density [15, 16]. Through numerical modelling, it was demonstrated that the spatial structure of the obtained atmospheric pressure glow discharge is very similar to that of low-pressure glow discharges displaying cathode fall, negative glow, positive column and anode layer regions. Nonetheless, the dielectric barrier limits the current and does not allow for a full transition to a normal glow discharge [16]. Often, in this context, the glow discharge is referred to as a sub-normal glow. Martens *et al*. concluded that an intermediate regime between Townsend and glow discharges is also possible [17]. A modelling study of a DBD in Xe shows that space charge formation is caused by a fast increase in the ionization rate due to stepwise ionization [18]. Interestingly, Adamovich *et al* developed an analytic 1D model for repetitively pulsed nanosecond discharges in dry air in the presence of a dielectric barrier. Among other physical parameters, the developed analytic model was able to predict the electric field distribution in the plasma and in the sheath as well as the sheath location [19], in excellent agreement with experimental data collected using four-wave mixing [20]. Wang *et al* reported simulations of an atmospheric pressure DC micro-plasma in helium between metal parallel plates, a discharge without dielectric barrier. The simulations showed a similarity of the *pd* scaling law (pressure – sheath size) for the atmospheric pressure micro-plasma with the often-reported scaling laws for low pressure glow discharges [21].

From a fundamental perspective, electric field profiles in the sheath are essential for determining sheath properties as the electric field provides direct information of the space charge responsible for the sheath structure. Knowledge of the electric field in the sheath advances the study of discharge nonlinearities and contributes to testing plasma models and sheath theories. Understanding sheath formation and identifying conditions for stable glow discharge formation and instabilities have the potential to enable advances in diffuse discharge formation at atmospheric pressure with an enhanced control capability for plasma-substrate interactions.

Many *in-situ* and non-intrusive techniques have been previously employed for electric field measurements. At low pressures, most of the laser techniques rely on probing the electric field-induced Stark shifting and mixing of the atomic or molecular Rydberg states using optogalvanic [6,22] or fluorescence detections [23,24]. Such techniques can measure field strengths as low as 10 V/cm when using probe species such as NaK or BCl [5]. A fluorescence detection instead of the optogalvanic detection enables improved temporal and spatial resolution. Czarnetzki *et al* developed another approach to measure electric fields in plasmas named fluorescence dip spectroscopy [11]. Despite being powerful to probe electric fields at low pressures, the previously listed diagnostic techniques suffer from fluorescence trapping and from the overlapping of Stark components of the Rydberg states at higher pressure due to collisional broadening. This led to the development and implementation of other diagnostics for electric field measurements that are compatible with a high collisional environment. One approach is electric field-induced coherent Raman scattering (CRS), a technique that is favorably applied at elevated pressures. Electric field-induced CRS has been applied by several researchers to investigate different plasmas [14,25,26]. Nonetheless, the technique is limited to Raman active gases and has been mainly used in N_2 and H_2 plasma. More recently, electric field-induced second harmonic (EFISH) generation has shown to be a powerful and versatile technique for electric field measurements in plasmas. The only requirement is that the gas has a reasonable polarizability and so can be used in most high-pressure plasmas. The time resolution of the measurement is limited only by the laser pulse duration. Unlike CRS, EFISH is species-independent and can be self-calibrating [27,28]. In spite its lower sensitivity in He (due to the small polarizability of He) EFISH was successfully applied to measure electric fields in atmospheric pressure He plasma jets [29]. Nonetheless, many of the reported EFISH measurements have been performed in highly complex electrode geometries and in non-homogeneous molecular plasmas making the fundamental analysis of the results and sometimes even the interpretation of the measured line integrated electric field challenging [29,30].

A range of different optical emission diagnostics have been developed for electric field measurements. Stark polarization emission spectroscopy is a relatively simple technique for the determination of electric fields for light atoms such as H and He. It is based on the polarization-dependent Stark splitting and shifting of atomic emission lines. The wavelength distance between the components is determined by the local electric field strength and the radiation from the plasma is polarized in the axial electric field direction [31]. This method has been applied to different plasmas [31-33]. Stark splitting of a hydrogen Balmer line has been similarly used for the measurement of the E-field in the cathode layer of a dc glow discharge [34].

Electric field measurements can in principle be obtained from line ratio methods as excitation in plasmas is highly dependent on the reduced electric field. For instance, using the ratio of the singlet lines at 667.8 nm and 728.1 nm Ivkovic *et al* performed 1D measurements of the electric field in the cathode fall of a 16 kHz atmospheric pressure dielectric barrier discharge in helium [35]. However, line-ratio techniques have always a limited validity range and require a detailed

collisional-radiative model to include collisional processes that impact the emission intensity in high pressure plasmas.

In this work, we report time and spatially resolved axial electric field measurements in the cathode fall region of a nanosecond pulsed helium discharge in a parallel plate geometry at 120 Torr. The measurements are performed using nanosecond time-resolved Stark polarization spectroscopy. The experimental results are compared with results from a 1-D fluid model enabling to discuss the mechanisms behind the space charge formation.

2. Experimental setup and Stark polarization spectroscopy

Figure 1 shows a schematic of the experimental setup including an image of the plasma discharge in operation. The discharge is generated between two parallel aluminum plate electrodes (22 mm × 13 mm) separated by a 3.5 mm gap. The gap distance is fixed using two plastic spacers placed between the supports of the upper and lower electrodes (see figure 1(b)). These spacers are positioned a few millimeters from the plasma region to avoid any disturbance of the plasma. The electrodes are enclosed in a vacuum vessel with ample optical access to the discharge area. High-purity (99.9995% pure) helium gas flows through the vacuum vessel with a flow rate fixed at 1 standard liter per minute (slm), controlled by a mass flow controller to avoid the accumulation of impurities. The pressure inside the vacuum cell was kept at 120 Torr. This was achieved by an adjusted needle valve inserted between the vacuum chamber and the vacuum pump (Edwards nXDS6i) and monitored with a piezoelectric pressure transducer (MKS Instruments 902B-11010). The vacuum vessel was mounted on a three-axis translation stage to enable precise alignment of the setup with the optical diagnostics.

The electrodes were connected to high voltage vacuum feedthroughs mounted on the vacuum vessel to allow for grounding and suppling high voltage pulses. The upper electrode from figure 1(a) was powered by an externally triggered high voltage pulse generator (DEI PVX-4130), which produced positive square voltage pulses with an amplitude of 1.3 kV, a pulse width of 200 ns and a repetition frequency of 4 kHz. The lower electrode was grounded. The pulse generator was fed by a high voltage power supply (Spellman SL150) and the pulse width and repetition frequency were controlled by a function generator (Tektronix AFG2021). The voltage and current waveforms were measured with a high voltage probe (Tektronix P6015A) and a Rogowski coil (Pearson electronics 2877) connected to a digital oscilloscope (LeCroy WaveSurfer10) with a 1 GHz bandwidth.

Figure 1 shows the optical detection system used for electric field measurements using Stark polarization spectroscopy which is identical to the setup used in [36]. Two plano-convex lenses (f_1 = 180 mm and f_2 = 100 mm) were used to project the plasma emission on the entrance slit of a 1-m focal length Czerny-Turner spectrometer (Acton Research Corporation, model AM-510) equipped with a 1800 grooves mm^{-1} grating. The slit width was fixed at 50 μm. A plastic plate linear polarizer on a rotation mount was inserted between the imaging lenses and the entrance slit of the spectrometer to ensure the collection of only π-polarized radiation. The polarizer is oriented so that only vertically polarized light is transmitted, enabling the measurement of electric field components perpendicular to the surface of the electrodes. The spectrometer was backed by an Intensified charge coupled device (ICCD, Andor Technology, iStar DH340T) consisting of 512 x 2048 pixels (pixel dimension: 13.5 μm x 13.5 μm). The present configuration yields a spectral resolution of about 40 pm (Gaussian instrumental function) as measured by the mercury line at 546 nm from a low-pressure mercury-argon pen lamp. The ICCD is externally triggered by the

TTL output of the same signal generator triggering the high voltage pulse generator and time-resolved measurements are performed using the internal delay generator of the ICCD camera. The gate size is fixed at 3 ns and each data point consists of an accumulation of about 4×10^5 to 2.4×10^6 spectra. The spectra are on chip accumulated and not binned. The spatial resolution of the present measurement is 22 μm (corresponding to 1 pixel). In this work, we used Stark polarization spectroscopy to measure the evolution of the electric field during the plasma pulse. Particularly we used the He I ($2p^1P^0 - 4d^1D$) transition with its forbidden component He I ($2p^1P^0 - 4f^1F$) emitting at 492.2 nm. We used the π-polarized components (in the direction of the electric field and perpendicular to the electrode surface) for Stark shifting [33]. The electric field strength as a function of the distance between the allowed transition and its forbidden counterpart for the transitions at 492.2 nm is given by [36]:

$$E = (-58.557 + 18.116 \times \Delta\lambda_{AF} + 3130.96 \times \Delta\lambda_{AF}{}^2 + 815.6 \times \Delta\lambda_{AF}{}^3)^{0.5} \qquad (1)$$

where E indicates the electric field strength in units $kVcm^{-1}$ and $\Delta\lambda_{AF}$ the distance between the peaks of the allowed and forbidden lines in units nm. Equation (1) is valid for electric field values between 1 and 100 kV cm^{-1}. To determine the electric field, we performed a fit of the line profile using three line profiles to represent the allowed, forbidden and *field-free* lines. The uncertainty on the electric field values inferred from the fit is estimated by evaluating the upper and lower bounds of electric field values for which the fits satisfy $R^2 > 0.95$. R^2 being the coefficient of determination of the fit obtained from the fit residual norm. This approach is described in detail in [36]. All the spectroscopic measurements were performed by imaging the middle of the discharge onto the vertical slit of the spectrometer.

3. Fluid model

The Townsend to glow transition in the parallel plate nanosecond pulsed discharge in helium was investigated using a one dimensional (1D) multi-species and multi-temperature fluid model. The 1D assumption is justified by the uniform and diffuse nature of the discharge in the early phase evident from ICCD images that are presented in the result section. The computational domain is the 3.5 mm gap distance. The pressure and temperature of the background helium gas (He) are assumed to be 120 Torr and 300 K, respectively.

The fluid model used in the present work includes time dependent continuity equations with drift-diffusion flux approximation for neutral species (He ground state atoms, He* excited metastable atoms ($He(2^1S)$ and $He(2^3S)$), and He_2* excited metastable molecules: $He_2(a^3\Sigma_u^+)$), electrons, and ions (He^+ and He_2^+).

$$\frac{\partial n_i}{\partial t} + \nabla \cdot \mathbf{\Gamma}_i = \sum_j R_{ij}\,, \mathbf{\Gamma}_i = \mathrm{sgn}(q_i) n_i \mu_i \boldsymbol{E} - D_i \nabla n_i \;\#(2)$$

n_i is the species density for species with index label i. $\boldsymbol{\Gamma_i}$ is the species drift-diffusion flux and R_{ij} the species generation rate through gas phase chemical reactions with other species j. D_i, μ_i, and $\boldsymbol{E}$ are the species diffusivity, mobility and the electric field. q_i being the charge number of the particle i, sgn(q_i) is positive (+) for ions, negative (-) for electrons and nil for neutral species.

The continuity equations are coupled with the electron energy equation and Poisson equation

$$\frac{\partial (n_e \varepsilon)}{\partial t} + \nabla \cdot \left(\frac{5}{3} \varepsilon \mathbf{\Gamma}_e - \frac{5}{3} n_e D_e \nabla \varepsilon \right) = -e \mathbf{\Gamma}_e \cdot \boldsymbol{E} - \sum_j \Delta E_j K_{inel,j} - 3 \frac{m_e}{m_{He}} K_{el} k_b (T_e - T_g) \#(3)$$

$$-\varepsilon_0\nabla^2\Phi = \varepsilon_0\nabla\cdot\boldsymbol{E} = \sum_j q_j n_j \quad \#(4)$$

with ε, $\boldsymbol{\Gamma}_e$, D_e, e, $K_{inel,\,j}$, ΔE_j, m_e, m_{He}, K_{el}, k_b, T_g ε_0 and Φ, the electron mean energy, electron drift diffusion flux, electron diffusivity, elementary charge, rate coefficient for inelastic collisions of electrons with species j, the energy exchange during inelastic collisions, electron mass, gas species mass, electron-neutral transfer frequency, Boltzmann constant, gas temperature, vacuum permittivity and electric potential, respectively. We do not solve the energy equation for heavy particles and assume that their temperature is equal to the gas temperature during the first 50 ns of the voltage pulsed that was modelled. Equations (2)-(4) are solved using the finite element method of the COMSOL Multiphysics software.

Table 1 shows the list of reactions included in the model together with their reaction rate coefficients. In the model, ionization of He atoms occurs by electron impact from the ground electronic state and by stepwise ionization of excited metastable states. Electron–electron collisions and superelastic collisions of electrons with He^* metastable atoms have been neglected because of the low electron density during the early stages of the discharge development. The reaction rate coefficients for the electron impact reactions are included as functions of the mean electron energy in COMSOL. The transport coefficients (mobility and diffusivity) for electrons and reaction rate coefficient for reaction 1, 2 and 3 were computed using BOLSIG + [37] using the cross sections set from the Morgan database on the open access LXCat website [38]. The diffusion coefficients for ions and neutrals are computed using the Chapman-Enskog theory combined with mixture-averaged diffusion formulation [39]. Ion mobility was calculated from their diffusion coefficients using the Einstein relation [40].

Table 1 Reactions set considered in the model together with their rate coefficients.

No.	Reactions	Rate coefficient (m^3s^{-1}, m^6s^{-1})	Energy cost (eV)	Ref.
1	e+He→e+He	$f(\varepsilon_{avg})$	0	[41]
2	e+He→e+He^*	$f(\varepsilon_{avg})$	19.8	[41]
3	e+He→2e +He^+	$f(\varepsilon_{avg})$	24.58	[41]
4	e+He^*→e+He	$1.7633\times10^{-16}\varepsilon_{avg}^{0.31}$	-19.8	[42]
5	e+He^*→2e+He^+	$1\times10^{-13}\varepsilon_{avg}^{0.6}\exp(-7.175/\varepsilon_{avg})$	4.78	[42]
6	e+He_2^*→2e+He_2^+	$7.28\times10^{-16}\varepsilon_{avg}^{0.71}\exp(-5.1/\varepsilon_{avg})$	3.4	[42]
7	2e+He^+→e+He	$7\times10^{-32}T_{eg}^{-4.5}$	/	[43]
8	2e+He_2^+→e+2He	$7\times10^{-32}T_{eg}^{-4.5}$	/	[43]
9	e+He+He_2^+→3He	$2\times10^{-39}T_{eg}^{-2.5}$	/	[43]
10	e+He+He_2^+→2He+He^*	$5\times10^{-39}T_{eg}^{-1}$	/	[43]
11	2e+He^+→e+He^*	$6\times10^{-32}T_{eg}^{-4}$	/	[43]
12	e+He_2^+→He^*+He	$1\times10^{-32}T_{eg}^{-4}$	/	[43]

13	$2e+He_2^+ \rightarrow e+He_2^*$	$3\times10^{-32}T_{eg}^{-4}$	/	[43]
14	$e+He_2^+ \rightarrow He+He^*$	$8.9\times10^{-15}T_{eg}^{-1.5}$	/	[43]
15	$He^*+2He \rightarrow He_2^*+He$	1.3×10^{-45}	/	[42]
16	$He^++2He \rightarrow He_2^++He$	1×10^{-43}	/	[42]
17	$2He^* \rightarrow He+e+He^+$	2.7×10^{-16}	/	[43]
18	$2He^* \rightarrow e+He_2^+$	1.05×10^{-15}	/	[44]
19	$He_2^*+He^* \rightarrow 2He+e+He^+$	5×10^{-16}	/	[43]
20	$He_2^*+He^* \rightarrow He+e+He_2^+$	2×10^{-15}	/	[43]
21	$2He_2^* \rightarrow 3He+e+He^+$	3×10^{-16}	/	[43]
22	$2He_2^* \rightarrow 2He+e+He_2^+$	1.5×10^{-15}	/	[44]
23	$2He+He^* \rightarrow He+He_2*$	2×10^{-46}	/	[44]
24	$He_2^*+He \rightarrow 3He$	4.9×10^{-22}	/	[43]

*ε_{avg} (eV) is the average electron energy. T_e (eV) is the electron temperature. T_{eg} is the electron temperature divided by the gas temperature.

The boundary conditions imposed on the electrodes are as follows. Flux boundary conditions of electrons and electron energy at the solid surfaces are given by the following equations [45,46]:

$$\boldsymbol{\Gamma}_e \cdot \boldsymbol{n} = \frac{1}{2} n_e \sqrt{\frac{8k_b T_e}{\pi m_e}} - \alpha_s n_e \mu_e \boldsymbol{E} \cdot \boldsymbol{n} - \sum \gamma_i (\boldsymbol{n} \cdot \boldsymbol{\Gamma}_i) \quad \#(5)$$

$$\boldsymbol{n} \cdot \boldsymbol{\Gamma}_\varepsilon = \frac{5}{6} n_\varepsilon \sqrt{\frac{8k_b T_e}{\pi m_e}} - \alpha_s n_\varepsilon \mu_e \boldsymbol{E} \cdot \boldsymbol{n} - \sum \gamma_i \varepsilon_i (\boldsymbol{n} \cdot \boldsymbol{\Gamma}_i) \quad \#(6)$$

where $\boldsymbol{n}$ is the normal pointing towards the solid surface, m_e is the electron mass, γ_i and $\varepsilon_i$are the secondary electron emission coefficient and the mean energy of secondary electrons emitted from the cathode electrode of species i, respectively. α_s is depends on the product of $\boldsymbol{E}$ and $\boldsymbol{n}$ as Equation (7), so that the field-driven ion flux at the surface is non-zero only when the electric field directs ions into the surface.

$$\alpha_s = \begin{cases} 1 (\mathrm{sgn}(z_i)\boldsymbol{E} \cdot \boldsymbol{n} > 0) \\ 0 (\mathrm{sgn}(z_i)\boldsymbol{E} \cdot \boldsymbol{n} \leq 0) \end{cases} \#(7)$$

where z_i is the charge of the considered species. The flux of heavy ions and metastables at the electrodes are given by:

$$\mathbf{n} \cdot \boldsymbol{\Gamma}_i = \frac{1}{4} n_i \sqrt{\frac{8k_b T_i}{\pi m_i}} + \alpha_s \mu_i n_i \boldsymbol{E} \ \#(8)$$

where m_i is the mass of the heavy ions and metastables. T_i is the temperature of heavy ions, and it is assumed to be equal to the gas temperature T_g. The second term on the right-hand side of equation (8) represents the loss of ions due to the movement driven by the electric field, and it is zero for the neutral species. The secondary electron emission coefficient for ions (He^+ and He_2^+)

varied from 0.005 to 0.25 in literature [45,47]. Our simulation results show that the discharge current magnitude increases with the secondary emission coefficient, and the simulated current magnitude is in best agreement with the measured current magnitude when the secondary electron emission coefficient is 0.135. The initial densities of electron and ions (He^+ and He_2^+) are set to be 10^{10} m^{-3}, 5×10^9 m^{-3}, and 5×10^9 m^{-3}, respectively. The experimental voltage waveform at the anode is applied as voltage boundary condition. We modelled first a voltage pulse and let the plasma produced species recombine for 250 μs, the time at which the subsequent voltage pulse is applied in the experiment. The species densities obtained at the end of this simulation were introduced as initial conditions in the second period to consider for pre-ionization that leads to a pulse-to-pulse memory effect. A steady-state solution is obtained after four discharge periods, and all results presented in this paper are from the fifth discharge period.. Different time steps were used in the model for the voltage pulse and the inter-pulse time. Based on the Courant Friedrichs Lewy (CFL) criterion, the maximum time step was set to be 10^{-12} s during the voltage pulse, and it was 10^{-8} s during the inter-pulse time. Under the constraint of the maximum time step, time steps are automatically determined by specified relative (0.001) and absolute (0.001) tolerances. The tolerances control the allowable error in each integration step in a way that the step is accepted if the estimated local errors satisfy both tolerances. A minimum mesh size 0.6 μm was used near the anode and cathode electrodes and the mesh size was increased following a geometric progression to 5 μm in the middle of the gas gap. The calculation consisted of a total of 1500 mesh elements in the 3.5 mm discharge gap.

4. Results and discussion

Figure 2 shows the experimentally measured voltage and current waveforms. The maximum voltage and current are about 1.3 kV and 8 A, respectively. The current waveform has a FWHM of about 70 ns. The first two peaks in the current waveform are due to the displacement current with a maximum of 0.7A. The displacement current is neglegible for the remainder of the voltage pulse. The voltage is decreasing with increasing current and starts to decrease much faster at t=0 s, the time corresponding to the maximum of the current. This fast reduction in voltage causes a significant reduction in the discharge current. The coupled pulse energy is about 0.6 mJ, however during the initial development before t = -50 ns, the time domain of interest for the development of the space charge region, only 57 μJ of energy is dissipated. Figure 2 also shows the current waveform predicted by the kinetic model, using the experimental voltage waveform as input. The solid line, part of the current waveform up to t = -50 ns corresponds to the time domain of interest for the present study. While the model can reproduce the shape and amplitude of the experimental current waveform, the plasma conditions for t > -50 ns lead to a very thin sheath and excessive large electric field which are not consistent with the local field approximations made in the model. Other observed differences between the measured and predicted current waveforms could arise because the fluid model cannot account for stochastic variations and effects of impurities on the pre-ionization, which were previously shown to be of importance during the initiation stage of the discharge development [48,49,50].

Figure 3 shows time resolved broadband ICCD plasma emission images illustrating the dynamics of the discharge development. Figures 3(a)-(b) are taken with a large camera gate (1 μs) enabling to record all the plasma emission produced during the entire discharge pulse. Figure 3(a) displays a single-shot image while figure 3(b) is averaged over 50 discharge pulses, nonetheless the images are nearly identical showing that the investigated discharge has a good shot to shot reproducibility. The large intensity near the cathode suggests the presence of a near cathode space charge region

while the near anode region has an increased intensity exhibiting non-uniformity. The entire discharge pattern is consistent with the emission pattern of an atmospheric pressure glow discharge [15,48,51].

Nonetheless, the dynamics of the discharge shows some atypical features of a glow discharge. Figure 3(c) shows the dynamics of the discharge with a 5 ns camera gate, the signal accumulated over 20 discharge pulses each. It is readily apparent that the discharge develops as a cathode-directed diffuse ionization wave. At t = -80 ns the weak emission front of the ionization wave is located about 1 mm from the anode, near the mid-gap position. At t = -75 ns, the ionization has gained intensity and the front is located about 0.6 mm above the cathode surface. 5 ns later the ionization front has reached the cathode and a bright emission zone near the cathode is formed. At longer time scales, an increase in intensity near the anode is observed which triggers the launch of a second ionization wave towards the cathode. However, this second ionization wave never reaches the cathode and its development is accompanied with plasma instabilities as illustrated by the formation of filamentary structures extending from the anode into the discharge gap. These filaments have a typical radius around 300 μm result most likely from an anode instability. Such instabilities occurring in the vicinity of the anode were observed by Akishev *et al*, in pin-to-plane discharges in air at high pressures (up to atmospheric pressure) during a glow-to-spark transition [52,53]. The high current density anode spots are triggered by the presence of high electric fields in the anode layer and the negative differential resistance of the layer which is prone to instabilities [2,52,53]. The plasma emission intensity near the high-voltage electrode increases due to the presence of the filaments formed from the anode spots. Simultaneously, the light intensity near the cathode increases, resulting in a dark intermediate area from t = -40 ns onward. The growth of the high intensity filamentary anode part is limited by the duration of the pulse which prevents excessive heating and a thermal ionization instability which will lead to spark formation for larger pulse widths [2]. The remainder of the paper is focused on the diffuse and uniform discharge for t < -50 ns.

Figure 4 plots the time evolution of the spatial profiles of emission at 492.2 nm of the He I (2^1P – 4^1D) transition recorded through the spectrometer with a 3 ns camera gate. The ionization wave reaches the cathode within about 9 ns consistent with the image in figure 3 (c). This corresponds to an average speed of about 4×10^5 m s^{-1}. The dynamics of the changes in light intensity within the gap are more apparent, including the decrease in light intensity after the ionization wave reached the cathode and the near cathode space charge region is formed. At the current peak (t = 0), most of the light collected originates from the bright cathode layer. Similar spatial structure and discharge dynamics were observed by Luo *et al* for an atmospheric pressure AC-driven dielectric barrier discharge in helium between two parallel plates [51]. The diffuse and uniform emission was attributed to a Townsend discharge and the transition to inhomogeneous emission patterns was associated with a Townsend to a subnormal glow discharge. The dielectric barrier prevents the transition to a normal glow discharge because of the charging of the dielectric which reduces the electric field in the electrode gap and leads to a reduction in the discharge current. Because of this reduction in the electric field, the second cathode directed ionization wave and near anode instabilities were not observed in the case of a dielectric barrier discharge [51]. Similarly, Huang *et al* [48] observed the same dynamics for a nanosecond pulsed discharge in helium at atmospheric pressure sustained between two parallel plate metal electrodes separated by a 1 mm gap. However, because of the combined effects of the small discharge gap and the larger speed of ionization waves at increased pressure the time resolution of their imaging apparatus, might not have allowed to capture the dynamics of the secondary ionization wave.

Figure 5 shows Stark polarization spectra recorded in the gap near the cathode, during the discharge at different moments in time, together with fits of the allowed, forbidden and field free line components following the procedure detailed in [36]. A reference field-free line was measured at the peak of the discharge current in the bulk plasma where the field is expected to be very low allowing to determine the line position (492.19 nm) and the line width (full width at half maximum, 60 pm). The electric field magnitudes were inferred from the line profile fits either from the distance between allowed and field-free spectral components at low field magnitudes (see e.g. figure 5(a)) or from the distance between the forbidden and allowed components for electric field amplitudes that lead to a significant forbidden line component (see figures 5(b)-(d)). The detection limit of the technique for the present conditions is estimated to be about 4-5 kV cm^{-1}. The unshifted field-free line appears to be the most prominent spectral component for all the depicted sample spectra. This is likely because our measurements are line of sight integrated and the electric field might have a non-uniform distribution along the line of sight due to the rounded electrode edges. The presence of high-intensity field-free lines in sheaths has been previously reported in sheaths of atmospheric pressure RF discharges and was attributed to the limited spatial resolution of the measurement [9,54]. Nonetheless for high electric field magnitudes, large wings of the Stark spectra are observed because of the significant shift of the allowed and forbidden components (see figure 5(c,d)). Wang *et al* suggested that for electric field values of several 10s of kV cm^{-1} another forbidden component ($2^1P - 4^1P$) appears however this line component has a larger shift than the spectral range shown in Figure 5 [9] and was not observed.

While the nitrogen impurity level was low enough not to observe significant nitrogen emission for times $t < 0$ ns, it was possible to measure the spectrum of the second positive system N_2 (C→B) (0,0) at the current peak. The gas temperature was inferred by comparing the measured spectrum with a synthetic spectrum from Specair [55] yielding a gas temperature of 310 ± 20 K. The minor gas heating is consistent with the combined low energy density coupled to the gas by the discharge. While the electric field is reported in this work, one can obtain the reduced electric field in good approximation assuming that the gas temperature remains at room temperature.

Figure 6(a) shows the experimental time-resolved electric field profiles as obtained from the experiment and the fluid model during the transition from the Townsend to the glow regime for times t as -77 ns ≤ t ≤ -50 ns. The intensity of the He emission line at 492.2 nm for t = -80 ns is too weak for determining the electric field during the cathode directed ionization wave. The increase in electric field occurs within 500 μm from the cathode. Moving forward in time during the propagation of cathode-directed the ionization wave, we observe that the thickness of the region with high electric field decreases from about 500 μm to 250 μm whereas the peak electric field obtained at the cathode increases from ~10-12 kV cm^{-1} to 40 kV cm^{-1}. The significant uncertainty on the electric field close to the cathode is due to the strong field-free component in the spectrum which significantly reduces the accuracy of fitting the forbidden and allowed lines (see also figure 5 (d)). While the model predicts the same trend and electric field amplitudes as the experiment, the model does not capture accurately the location of the sheath boundary.

An additional insight obtained from these modeling results is the reduction in the electric field at the sheath boundary compared to the electric field near the anode, which is consistent with the dark zone as observed in Figure 3. Actually, at t = -59 ns, 0.7 mm from the cathode an electric field reversal (negative electric field) is obtained. The electric field reversal at the edge of a sheath region, in the negative glow has been predicted by modeling calculations in a DC glow helium micro-plasma at atmospheric pressure [21] and in low pressures DC and RF discharges in argon

and helium [56]. Measurements of an electric field reversal were previously reported by Gottscho *et al* in low pressures DC discharges in argon and obtained by using laser optogalvanic detection [57]. Similarly, Schultze *et al* reported field reversals in RF discharges in argon using phase-resolved optical emission spectroscopy [58]. At atmospheric pressure, the electric field reversal was detected experimentally in the positive column of DBDs in air by four-wave mixing [26]. Electric field reversal in a negative glow region enables current continuity in the sheath region at high current density and is expected to be most significant at higher current densities as is the case in Figure 6(b).

The increase in electric field near the cathode is coinciding with a transition from a Townsend to a glow discharge due to an increasing electron density and hence the formation of a space charge region or cathode sheath. Most of the applied voltage is across the cathode sheath in a glow discharge, which for a 250 µm sheath would lead to a ~ 50 kV cm^{-1}, which is observed in the model while 40 kV cm^{-1} is observed in the experiment. Figure 6 (a) shows consistently that a reduction in sheath size by a factor 4 leads to an increase in the electric field at the anode by a factor 4. For t >-50 ns a rather fast and drastic reduction in sheath size was observed but the limited spatial resolution of the present diagnostic was not able to resolve the electric field profiles for these moments in time. The fast reduction in sheath size is consistent with the steep increase of the discharge current at t >-50 ns (see figure 2) suggesting a significant increase in electron density in the positive column.

The observed decrease in sheath thickness occurs within ~ 20-30 ns, a time scale at which the heavy ions remain static hence the formation of a space charge should be linked to enhancements in local ionization rates. Figure 7 shows the simulated spatio-temporal contour plots of the electric field (figure 7(a)), the electron density (figure 7(b)), the total ionization rate (figure 7(c)), and space charge density (figure 7(d)), respectively. The modeling results are plotted for -104 ns $\leq t \leq$ -50 ns. These modeling outcomes allow us to analyze the dynamics of the space charge formation in more detail. Figure 7(b) shows that the remaining electrons of the previous voltage pulse amount to an electron density of 5×10^{16} m^{-3} with a depletion near the electrodes. The found pre-ionization densities are similar to densities found in other studies [59]. Once a positive voltage is applied to the upper electrode around t ~ - 104 ns, the remaining electrons drift toward the high voltage electrode, decreasing the electron density near the cathode (figure 7(b)) and leading to an enhancement of the local electric field (see figure 7(c)). While a significant electron depleted region near the cathode is formed during that period, the electric field within the gap remains relatively uniform and low (< 1 kV cm^{-1} for t < -95 ns). Figure 7 (b) shows that a depletion of the electron density near the cathode occurs before the electron density increases in the bulk. This might suggest that the electrons remaining from the previous discharge pulse might facilitate sheath formation. The inhomogeneity in electron density leads to the formation of a sheath with enhanced ionization at the sheath edge. At that time, secondary electron emission upon ion impact does start to contribute to the process due to the enhanced electric field as a He^+ ion needs about 60 ns to cross a 250 µm sheath which is similar to the time scale of sheath formation. The increase of the ionization rate S_e at the sheath edge, results in the formation of a space charge density of similar magnitude as the electron density in the bulk of the plasma coinciding with a significant increase in the electric field (figure 7(a)). This ultimately does lead to an increase of the electron density in the bulk plasma. At t = -60 ns, $n_e \approx 2.4\times10^{17}$ m^{-3}, a factor of 5 higher than the pre-ionization level. This increase in electron density matches the observed gradual increase of the discharge current. The increase in electron density in the bulk plasma results in a decrease in the sheath thickness (see figure 7(d)) correlating with the expected decrease in the Debye length. With

most of the applied potential being across the sheath, a further increase in electric field in the sheath occurs which ultimately which lead to run away behavior if the applied voltage would not be reduced. Interestingly, experimentally an instability is found to develop at the anode (see above) and not at the cathode suggesting that the anode layer is more unstable at elevated pressure and current than the cathode sheath.

A cathode sheath in a dc driven discharge is responsible for the acceleration of electrons generated by ion-induced secondary electron emission on the metal cathode and hence the sustainment of the discharge [1]. Den Hartog *et al* reported spatially resolved electric field measurements in the cathode sheath of a dc driven helium discharge at 3.5 Torr between two metal electrodes (See Figure 1) [6]. Their results showed a linear decrease of the electric field in the cathode fall region consistent with the electric field in a matrix sheath. The non-homogeneous space charge (ion density) found in Figure 7 is inconsistent with a matrix sheath. The shape of the electric field found in Figure 6 is more like the electric field distribution found in a high current micro-glow discharge at atmospheric pressure by Wang *et al* [9]. The non-linear dependence of the electric field distribution in the sheath was found to be more pronounced for a larger discharge current density (~ 40 mA mm^{-2}) compared to the 13 mA mm^{-2} case of which the current density is more similar to the case investigated in this paper (~ 10 mA mm^{-2}). The collision-dominated high voltage ion sheath has an analytical solution referred to as the Mott-Gurney law or sheath model [60]. In this case, the electric field scales with $x^{1/2}$, x being the distance from the sheath edge, not unlike the electric field profile found in Figure 6. Similarly scaling the sheath thickness with the *pd* scaling law leads from a sheath thickness of 50 µm at atmospheric pressure to ~ 300 µm at 120 Torr similar to our findings. This scaling is however valid for a normal glow discharge [61]. With increasing current density, the electric field increases, and the sheath thickness reduces [61]. The rapid increase in current starting at ~ -50 ns leads to a rapid increase in the electric field and a collapse of the sheath thickness which requires diagnostics with higher temporal and spatial resolution than used in this work and hence is outside of the scope of this paper.

5. Conclusion

The dynamics of a nanosecond pulsed discharge in helium at 120 Torr between two metal electrodes was investigated using spatially and temporally resolved Stark polarization spectroscopy complemented with 1D fluid model. Time-resolved ICCD images show that during the breakdown process, the discharge transitions from a weakly luminous, diffuse and uniform cathode-directed ionization front to a glow discharge structure. The electric field measurements using the He I transition at 492.19 nm show the development of a space charge region near the cathode and are in excellent agreement with the modeling results. The space charge is generated on time scales of 20-30 ns by an enhanced ionization rate near the cathode which is self-enhanced by the coinciding increase of the electric field. The reduction of the sheath size with increasing current density results in a further increase of the electric field at the cathode. An electric field of 40 kV cm^{-1} due to accumulated space charge was measured 30 ns after the start of the Townsend discharge. Interestingly, while the largest ionization occurs near the cathode, the experiments show that an instability is developing near the anode as can been seen from the formation of filamentary structures that are growing towards the cathode over time.

Acknowledgments

This work was supported by the Department of Energy, office of Fusion Energy Science grant through the general Plasma Science Program under award number DE-SC0021376 and AT4010100. The work also heavily relied on methods developed and implemented in the framework of projects with award numbers DE-SC-0016053 and DE-SC-0020232. M.S.S. would like to thank Dr. Zak Eckert (Sandia National laboratories) for technical discussions. The authors acknowledge Mahsa Mirzaee for help with initial measurements in preparation of this work and the Minnesota Supercomputing Institute (MSI) at the University of Minnesota in providing resources that contributed to the results reported in this paper. Sandia National Laboratories is a multimission laboratory managed and operated by National Technology & Engineering Solutions of Sandia, LLC, a wholly owned subsidiary of Honeywell International Inc., for the U.S. Department of Energy?s National Nuclear Security Administration under contract DE-NA0003525. This paper describes objective technical results and analysis. Any subjective views or opinions that might be expressed in the paper do not necessarily represent the views of the U.S. Department of Energy or the United States Government.

References

1. Lieberman M A and Lichtenberg A J (2005) Principles of Plasma Discharges vol 2 (Hoboken, NJ: Wiley).
2. Bruggeman P J, Iza F and Brandenburg R (2017) Foundations of atmospheric pressure non-equilibrium plasmas, *Plasma Sources Sci. Technol*. 26 123002.
3. Pai D Z, Lacoste D A and Laux C O (2010) Transitions between corona, glow, and spark regimes of nanosecond repetitively pulsed discharges in air at atmospheric pressure *J. Appl. Phys*. 107 093303.
4. Lee D, Hershkowitz N and Severn G D (2007) Measurements of Ar^+ and Xe^+ velocities near the sheath boundary of Ar-Xe plasma using two diode lasers, *Appl. Phys. Lett*. 91 041505.
5. Gottscho R A (1987) Glow-discharge sheath electric fields: Negative-ion, power, and frequency effects. *Physical Review A*, *36*(5), 2233.
6. Den Hartog E A, Doughty D A and Lawler J E (1988) Laser optogalvanic and fluorescence studies of the cathode region of a glow discharge. *Physical Review A*, *38*(5), 2471.
7. Robertson S (2013) Sheaths in laboratory and space plasmas. *Plasma Physics and Controlled Fusion* 55 (9) 093001.
8. Gonzalez-Fernandez V, Grützmacher K, Steiger A, Pérez C and de la Rosa M I (2017) Measured cathode fall characteristics depending on the diameter of a hydrogen hollow cathode discharge. *Plasma Sources Sci. Technol.*, 26(10) 105004.
9. Wang Q, Koleva I, Donnelly V M and Economou D J (2005). Spatially resolved diagnostics of an atmospheric pressure direct current helium microplasma. *J. Phys. D: Appl. Phys.*, *38*(11), 1690.
10. Barnat E V and Hebner G A (2004). Electric fields in a sheath near a metal–dielectric interface. *Appl. Phys. Lett.*, 85(16), 3393-3395.
11. Czarnetzki U, Luggenhölscher D and Döbele H F (1999) Space and time resolved electric field measurements in helium and hydrogen RF-discharges. *Plasma Sources Science and Technology*, 8(2), 230.
12. Massines F, Gherardi N, Naude N and Segur P (2005) Glow and Townsend dielectric barrier discharge in various atmosphere. *Plasma Phys. Control. Fusion* 47 B577.
13. Luo H, Liang Z., Lv B, Wang X, Guan Z and Wang L (2007) Observation of the transition from a Townsend discharge to a glow discharge in helium at atmospheric pressure. *Appl. Phys. Lett.* 91, 221504.

14. Ito T, Kobayashi K, Czarnetzki U and Hamaguchi S (2010) Rapid formation of electric field profiles in repetitive high-voltage high-pressure nanosecond discharges, *J. Phys. D: Appl. Phys.* 43, 062001
15. Massines F, Rabehi A, Decomps P, Gadri R b, Segur P and Mayoux C (1998) Experimental and theoretical study of a glow discharge at atmospheric pressure controlled by dielectric barrier. *J. Appl. Phys.* 83, 2950–7.
16. Massines F, Segur P, Gherardi N, Khamphan C and Ricard A (2003) Physics and chemistry in a glow dielectric barrier discharge at atmospheric pressure: diagnostics and modelling. *Surf. Coat. Technol*. 174 8–14.
17. Martens T, Brok W J M, van Dijk J and Bogaerts A (2009) On the regime transitions during the formation of an atmospheric pressure dielectric barrier glow discharge. *J. Phys. D: Appl. Phys*. 42 122002.
18. Bogdanov E A, Kudryavtsev A A, Arsanbelkov R R and Kolobov V I (2004) Simulation of pulsed dielectric barrier discharge xenon excimer lamp. *J. Phys. D: Appl. Phys.* 37 2987–95.
19. Adamovich I V, Nishihara M, Choi I, Uddi M and Lempert W R (2009) Energy coupling to the plasma in repetitive nanosecond pulse discharges. *Phys. Plasmas* 16 113505.
20. Simeni Simeni M, Goldberg B, Gulko I, Frederickson K and Adamovich I V (2018) Sub-nanosecond resolution electric field measurements during ns pulse breakdown in ambient air *J. Phys. D: Appl. Phys.* 51 01LT01.
21. Wang Q, Economou D J and Donnelly V M (2006) Simulation of a direct current microplasma discharge in helium at atmospheric pressure. *J. Appl. Phys.* 100, 023301.
22. Doughty D K and Lawler J E (1984) Spatially resolved electric field measurements in the cathode fall using optogalvanic detection of Rydberg atoms. *Appl. Phys. Lett.*, *45*(6), 611-613.
23. Moore C A, Davis G P and Gottscho R A (1984) Sensitive, nonintrusive, in-situ measurement of temporally and spatially resolved plasma electric fields. *Phys. Rev. Lett.*, *52*(7), 538.
24. Greenberg K E and Hebner G A (1993) Electric-field measurements in 13.56 MHz helium discharges. *Appl. Phys. Lett.*, *63*(24), 3282-3284.
25. Ochkin V N, Savinov S Y, Tskhai S N, Czarnetzki U, Schulz-von der Gathen V and Döbele H F (1998) Non-linear optical techniques for plasma diagnostics, *IEEE Trans. Plasma Sci.* 26 1502–13.
26. Simeni Simeni M, Goldberg B M, Zhang C, Frederickson K, Lempert W R and Adamovich I V (2017) Electric field measurements in a nanosecond pulse discharge in atmospheric air *J. Phys. D: Appl. Phys.* 50 184002.
27. Dogariu A, Goldberg B M, O'Byrne S, and Miles R B (2017). Species-independent femtosecond localized electric field measurement. *Phys. Rev. Appl.*, *7*(2), 024024.
28. Chng T L, Orel I S, Starikovskaia S M and Adamovich I V (2019) Electric field induced second harmonic (E-FISH) generation for characterization of fast ionization wave discharges at moderate and low pressures. *Plasma Sources Sci. Technol. 28*(4), 045004.
29. Orr K, Tang Y, Simeni M S, van den Bekerom D and Adamovich I V (2020) Measurements of electric field in an atmospheric pressure helium plasma jet by the E-FISH method. *Plasma Sources Sci. Technol.*, *29*(3), 035019.
30. Simeni M S, Tang Y, Frederickson K and Adamovich I V (2018) Electric field distribution in a surface plasma flow actuator powered by ns discharge pulse trains. *Plasma Sources Sci. Technol.*, *27*(10), 104001.
31. Obradović B M, Ivković S S and Kuraica M M (2008) Spectroscopic measurement of electric field in dielectric barrier discharge in helium. *Appl. Phys. Lett.*, *92*(19), 191501.
32. Kuraica M M, Konjević N and Videnović I R (1997) Spectroscopic study of the cathode fall region of Grimm-type glow discharge in helium. *Spectrochim. Acta B*, *52*(6), 745-753.

33. Cvetanović N, Martinović M M, Obradović B M and Kuraica M M (2015) Electric field measurement in gas discharges using stark shifts of He I lines and their forbidden counterparts. *J. Phys. D: Appl. Phys.*, *48*(20), 205201.
34. Arkhipenko V, Kirillov A, Safronau Y, Simonchik L and Zgirouski S (2009) Self-sustained dc atmospheric pressure normal glow discharge in helium: from microamps to amps, *Plasma Sources Sci. Technol.* 18, 045013.
35. Ivković S S, Sretenović G B, Obradović B M, Cvetanović N and Kuraica M M (2014) On the use of the intensity ratio of He lines for electric field measurements in atmospheric pressure dielectric barrier discharge. *J. Phys. D: Appl. Phys.*, *47*(5), 055204.
36. Mirzaee M, Simeni Simeni M and Bruggeman P J (2020) Electric field dynamics in an atmospheric pressure helium plasma jet impinging on a substrate, *Phys. Plasmas 27, 123505*
37. Hagelaar G J M and Pitchford L C (2005) Solving the Boltzmann equation to obtain electron transport coefficients and rate coefficients for fluid models, *Plasma Sources Sci. Technol.* 14, 722.
38. Pitchford L C, Bartschat K, Biagi S F et al. (2017) LXCat: an Open-Access, Web-Based Platform for Data Needed for Modeling Low Temperature Plasmas*. Plasma Process. Polym*. 14, 160098.
39. Kee R J, Rupley FM, Miller J A, Coltrin M E, Grcar J F, Meeks E, Moffat H K, Lutz A E, Dixon-Lewis G, Smooke M D and Warnatz J (2003) Chemkin Collection, Release 3.7. 1. *Reaction Design, Inc., San Diego, California, USA*.
40. Ellis H W, McDaniel E W, Albritton D L, Viehland L A, Lin S L and Mason E A (1978) Transport properties of gaseous ions over a wide energy range, *At. Data Nucl. Data Tables* 22, 179–217.
41. Pitchford L C et al (2017) LXCat: an open-access, web-based platform for data needed for modeling low temperature plasmas, *Plasma Process. Polym.* 14 1600098.
42. Breden D, Miki K and Raja L (2012) Self-consistent two-dimensional modeling of cold atmospheric-pressure plasma jets/bullets, *Plasma Sources Sci. Technol.* 21, 034011.
43. Murakami T, Niemi K, Gans T, O'Connell D and Graham W G (2013) Chemical kinetics and reactive species in atmospheric pressure helium–oxygen plasmas with humid-air impurities, *Plasma Sources Sci. Technol.* 22, 015003.
44. Martens T, Bogaerts A, Brok W J M and Dijk J V (2008) The dominant role of impurities in the composition of high-pressure noble gas plasmas, *Appl. Phys. Lett.* 92, 041504.
45. Lazarou C, Belmonte T, Chiper A and Georghiou G (2016) Numerical modelling of the effect of dry air traces in a helium parallel plate dielectric barrier discharge, *Plasma Sources Sci. Technol.* 25 055023.
46. Hagelaar G J M, de Hoog F.J and Kroesen G M W (2000) Boundary conditions in fluid models of gas discharges*, Phys. Rev. E, 62(1) 1452-4*.
47. Sakiyama Y and Graves D B (2006) Finite element analysis of an atmospheric pressure rf-excited plasma needle, *J. Phys. D: Appl. Phys.* 39, 3451–6.
48. Huang B D, Takashima K, Zhu X M and Pu Y K (2015) The influence of the voltage rise rate on the breakdown of an atmospheric pressure helium nanosecond parallel-plate discharge J. Phys. D: Appl. Phys. 48 125202.
49. Eckert Z, Boerner J J, and Grillet A N (2019) 1D PIC-DSMC analysis of a high-pressure nanosecond pulse discharge breakdown in helium. *J. Phys. D: Appl. Phys.* 53(3) 035203.
50. Donkó Z, Hamaguchi S and Gans T (2019) Effects of excitation voltage pulse shape on the characteristics of atmospheric-pressure nanosecond discharges. *Plasma Sources Sci. Technol.* 28(7) (2019) 075004
51. Luo H, Liang Z, Lv B, Wang X, Guan Z and Wang L (2007) Radial evolution of dielectric barrier glow-like discharge in helium at atmospheric pressure. *Appl. Phys. Lett.* 91 231504.

52. Akishev Yu, Grushin M, Kochetov I, Karal'nik V, Napartovich A and Trushkin N (2005) Negative corona, glow and spark discharges in ambient air and transitions between them. *Plasma Sources Sci. Technol.* 14 S18–25.
53. Akishev Y, Karalnik V, Kochetov I, Napartovich A and Trushkin N (2014) High-current cathode and anode spots in gas discharges at moderate and elevated pressures. *Plasma Sources Sci. Technol.* 23 054013.
54. Navrátil Z, Josepson R, Cvetanović N, Obradović B and Dvořák P (2016) Electric field development in g-mode radiofrequency atmospheric pressure glow discharge in helium. *Plasma Sources Sci. Technol.* 25 03LT01.
55. Laux C (2002) Radiation and nonequilibrium collisional radiative models Physico-Chemical Modeling of High Enthalpy and Plasma Flows (von Karman Institute Lecture Series 2002–07) ed D Fletcher et al (Rhode-Saint-Genese: Specair) http://specair-radiation.net
56. Boeuf J P and Pitchford L C (1995) Field reversal in the negative glow of a dc glow discharge, *J. Phys. D: Appl. Phys*. 28 2083–8.
57. Gottscho R A, Mitchel A, Scheller G R and Chan Y (1989) Electric field reversals in dc negative glow discharges. *Phys. Rev. A* 40, 6407–14.
58. Schulze J, Donkó Z, Heil B G, Luggenhölscher D, Mussenbrock T, Brinkmann R P and Czarnetzki U (2008) Electric field reversals in the sheath region of capacitively coupled radio frequency discharges at different pressures, *J. Phys. D: Appl. Phys*. 41 105214.
59. Tholin F and Bourdon A (2013) Simulation of the stable quasiperiodic glow regime of a nanosecond repetitively pulsed discharge in air at atmospheric pressure Plasma Sources Sci. Technol. 22 045014
60. Benilov M S (2008) The Child–Langmuir law and analytical theory of collisionless to collision-dominated sheaths. *Plasma Sources Sci. Technol*. 18(1) 014005.
61. Raizer Yu P 1991 Gas Discharge Physics (New York, Berlin: Springer).

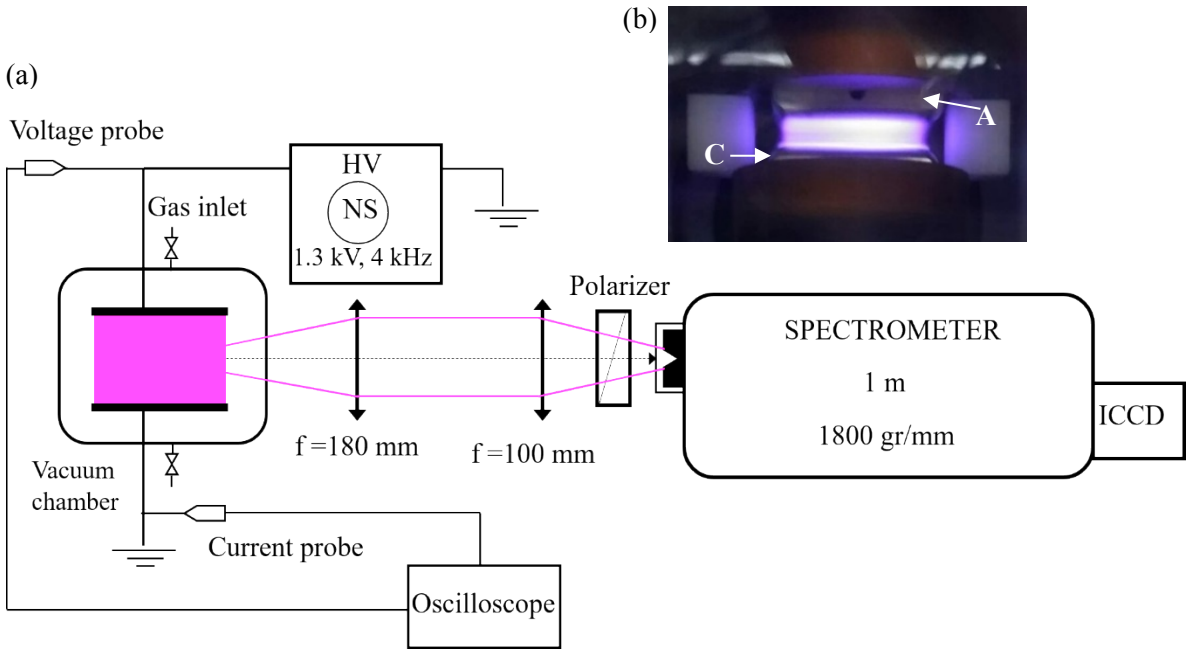


Figure 1. (a) Schematic of the plasma and the optical emission spectroscopy setup. (b) Photograph of the plate-to-plate discharge at 120 Torr. The gap distance is 3.5 mm.

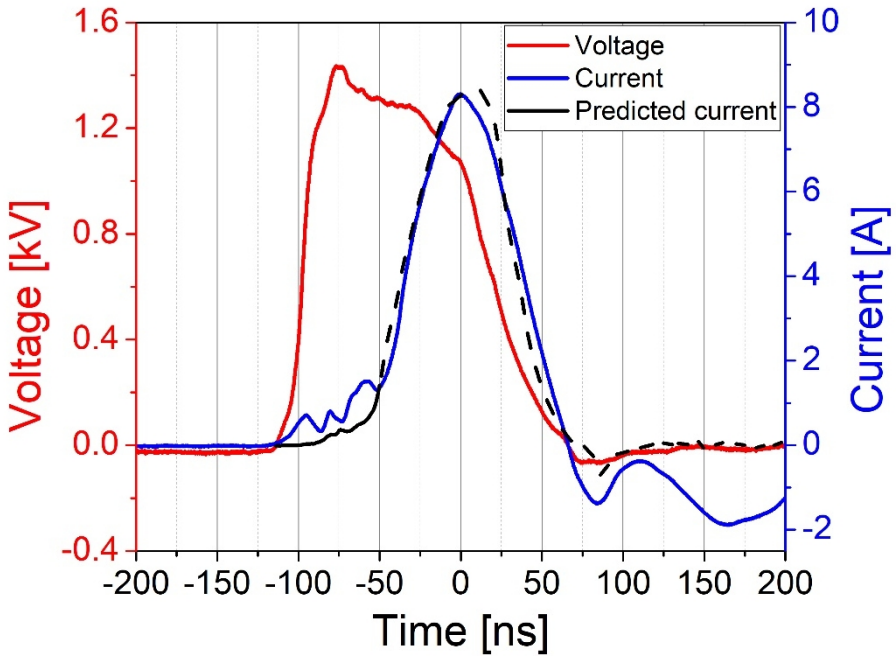


Figure 2. Experimental pulse voltage, current, and predicted current waveforms in the plate-to-plate discharge. The first two maxima in the current waveform are capacitive current.

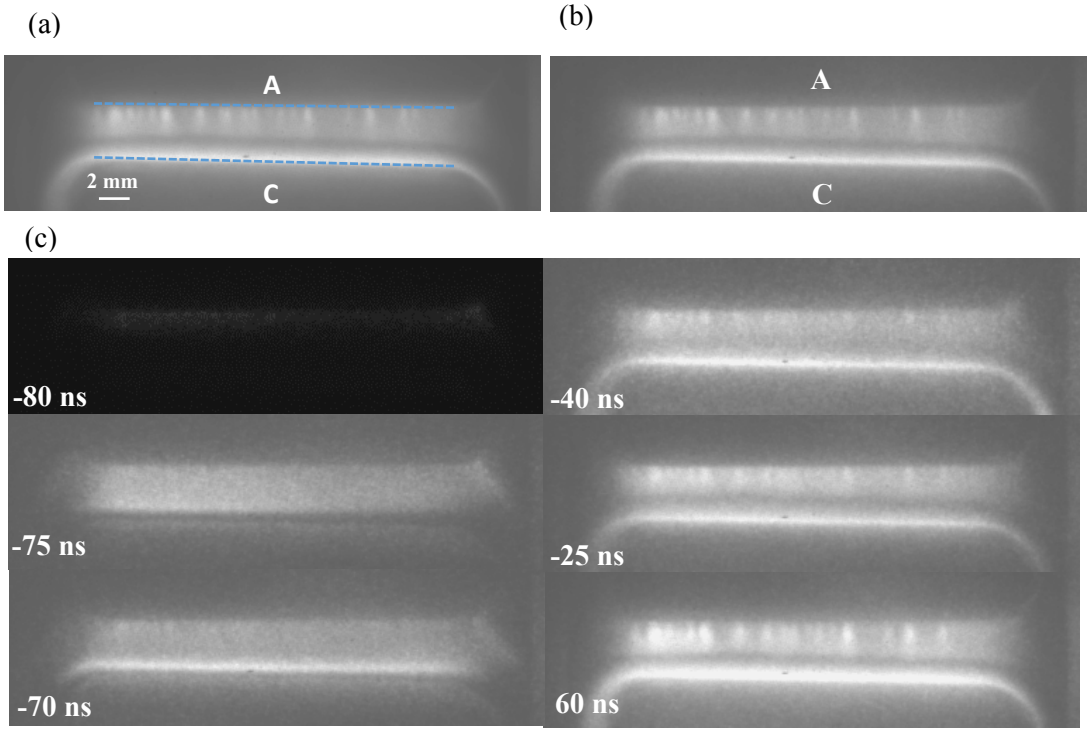


Figure 3. Broadband ICCD images of the parallel plate helium discharge. (a) Single-shot, 1μs gate. (b) 50-shots averaged, 1μs gate. (c) Time-resolved images with camera gate of 5 ns. Each image is an accumulation of 20 discharge pulses. The time delays relative to the moment when the peak of the current waveform occurs are shown in the images. The dash lines indicate the location of the electrodes surfaces.

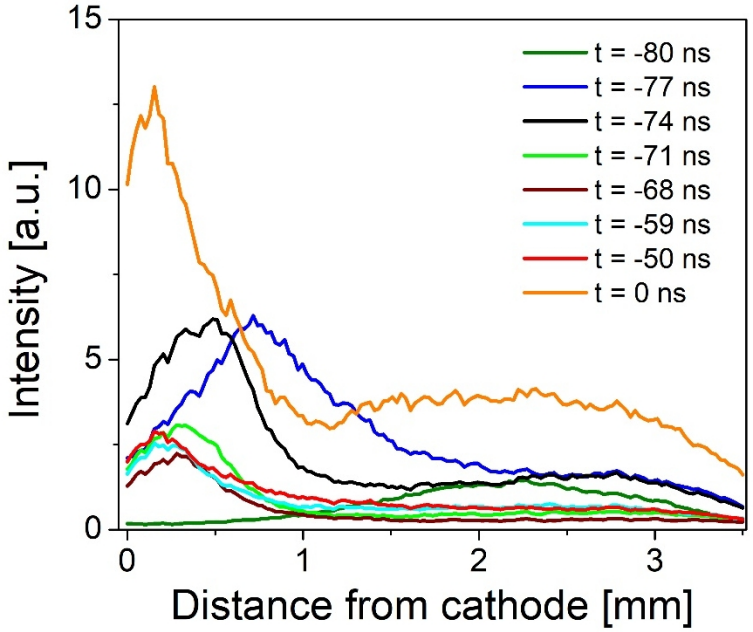


Figure 4. Relative intensity distributions of the 492.2 nm He line along the electrode gap. The camera gate is 3 ns. Peak intensity distribution for the corresponding times.

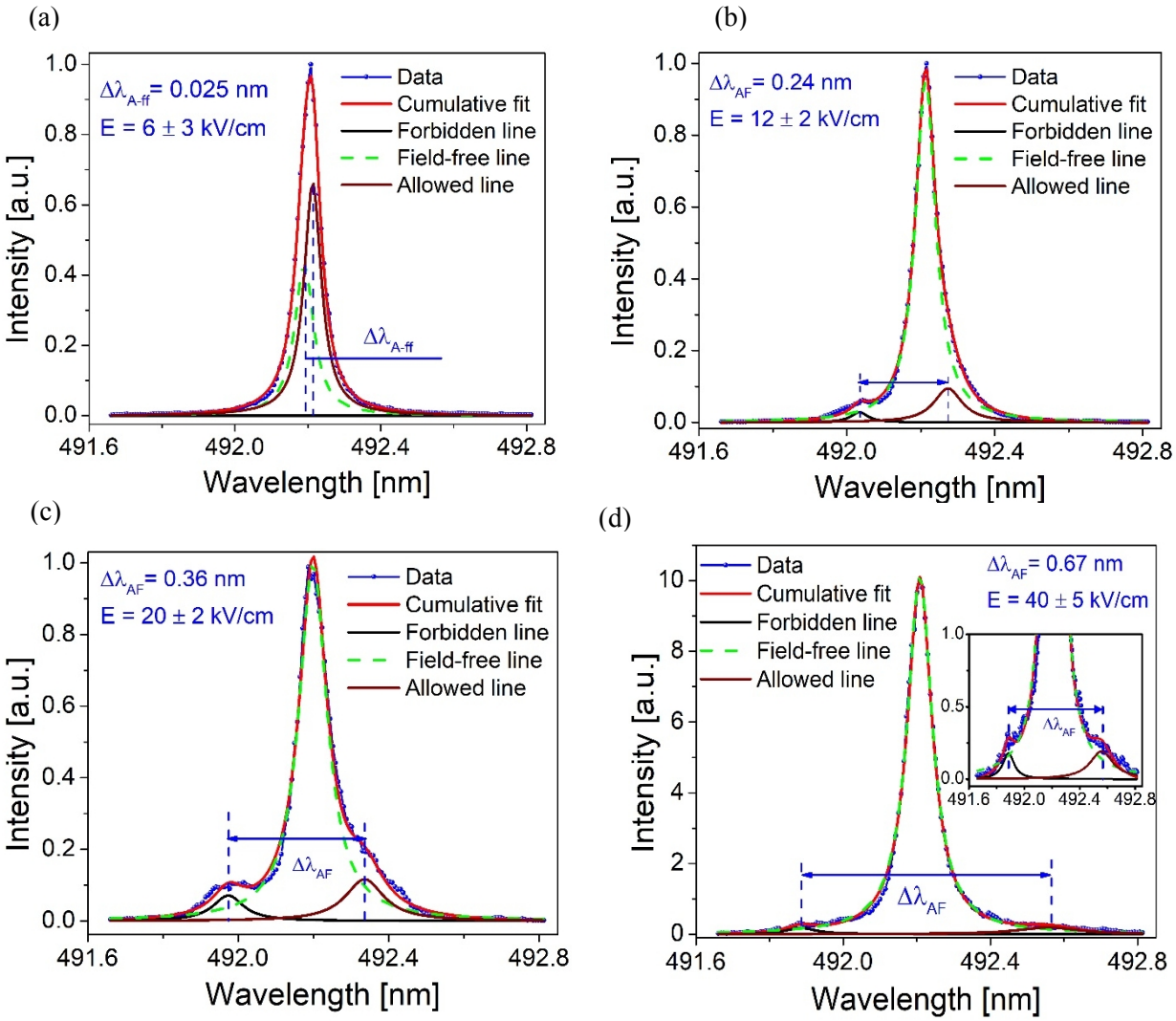


Figure 5. Stark polarization spectroscopy spectra recorded at 120 Torr for different moments in time and locations together with fits. The camera gate is 3 ns. (a) E = 6 ± 3 kV/cm. (b) E = 12 ± 2 kV/cm. (c) E = 20 ± 2 kV/cm. (d) E = 40 ± 5 kV/cm. $\Delta\lambda_{A\text{-}ff}$ is the distance between allowed and field-free lines. $\Delta\lambda_{AF}$ is the distance between allowed and forbidden lines.

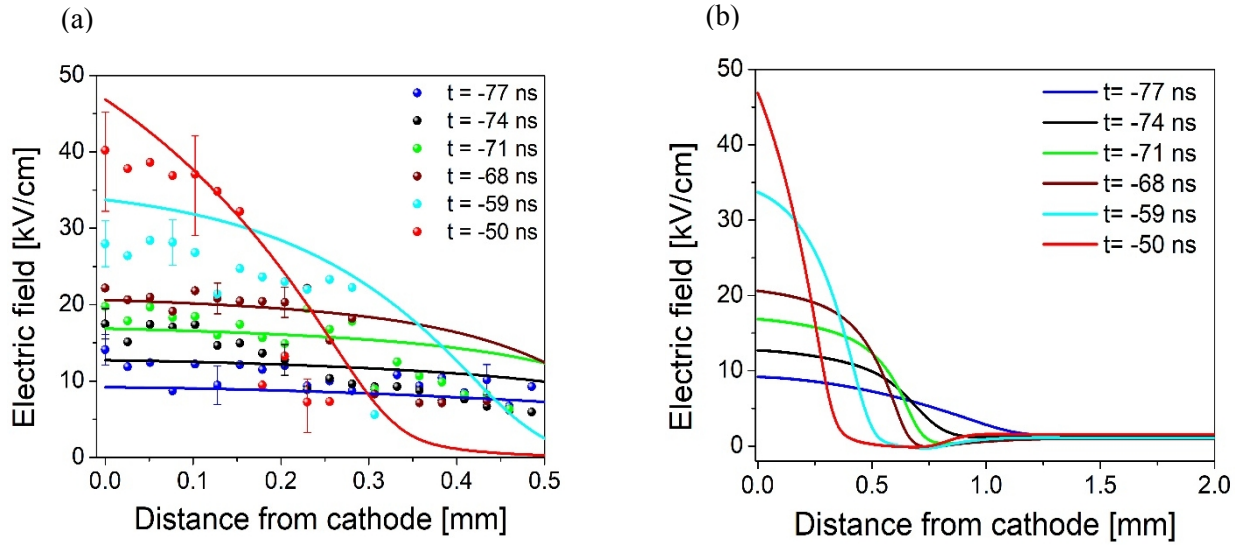


Figure 6. (a) Experimental and predicted electric field profiles during the voltage pulse for selected moments in time. (b) Electric field profiles as obtained from the fluid model. The axis on the experimental profile and model only covers 0.5 and 2 mm and the electrode gap distance is 3.5 mm.

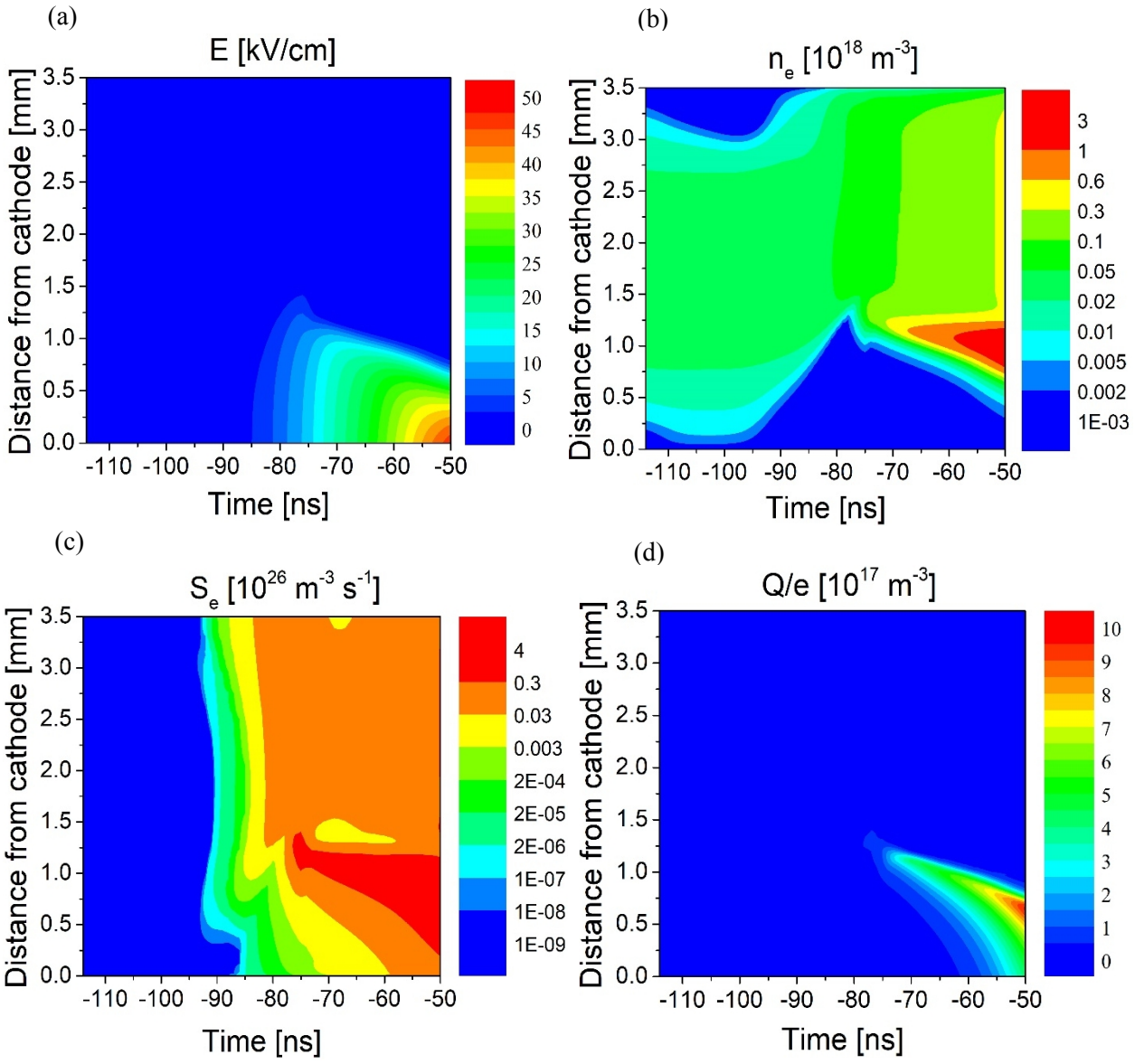


Figure 7. Calculated temporally and spatially resolved plasma properties with fluid model. (a) Electric field (E). (b) Electron densities (n_e). (c) Ionization rate (S_e). (d) Space charge density (Q).